ABSTRACT

Seismic Anisotropy in Texas and Oklahoma and Its Relationship
to Tectonic Events That Shaped Southern Laurentia

Cody Comiskey, M.S.

Chairman: Jay Pulliam, Ph.D.

We present new shear wave splitting measurements of approximately 1500 SKS phases recorded at 176 broadband seismic stations deployed in Texas and Oklahoma. SKS splitting on the North American (NA) craton show NE-SW fast axis polarization directions that are generally parallel to the average motion of the NA plate. Around the Southern Oklahoma Aulacogen the fast axis polarization direction changes to NW-SE and parallels the strike of the Aulacogen. Along the transition zone (COTZ), SKS phases show NE-SW polarization direction and parallel to the NA plate. However, larger delay times are observed on the COTZ. Observed patterns of fast axis directions parallel to plate motions, small delay times, and a shallower anisotropic depth are consistent with a lithospheric origin for the observed anisotropy on the craton. Larger delay times and a deeper anisotropic source suggest that asthenospheric flow is responsible for the seismic anisotropy observed along the COTZ.

Seismic Anisotropy in Texas and Oklahoma and Its Relationship to Tectonic Events That Shaped Southern Laurentia

by

Cody Comiskey, B.S.

A Thesis

Approved by the Department of Geology

_____

Steven G. Driese, Ph.D., Chairperson

Submitted to the Graduate Faculty of
Baylor University in Partial Fulfillment of the
Requirements for the Degree
of
Master of Science

Approved by the Thesis Committee

_____

Robert Jay Pulliam, Ph.D., Chairperson

_____

John A. Dunbar, Ph.D.

_____

Gregory A. Benesh, Ph.D.

Accepted by the Graduate School
August 2013

_____

J. Larry Lyon, Ph.D., Dean

Page bearing signatures is kept on file in the Graduate School.

TABLE OF CONTENTS

LIST OF FIGURES

ACKNOWLEDGMENTS

I would first like to thank my family for their support for my endeavor to further my education. No matter what the task at hand, my family always believed in my abilities, and for that I am forever grateful. I would like to thank my advisor Dr. Jay Pulliam for his continuous support, time and tutelage through this project, without him none of this would have been possible. Along with Dr. Pulliam, I want to thank the rest of my committee members Dr. John Dunbar and Dr. Greg Benesh for their time and input on my project. Along with my committee members I would like to thank the faculty and staff of the Baylor Geology department. They made me feel welcome from the very start and were always willing to lend an objective ear when questions and comments arose. A big thanks goes out to the rest of my fellow grad students, whom over the past two years I have become very close with. They were always willing to help when help was needed. I will always remember the great conversations that were conjured up on the couch in the geophysics lab, our afternoon excursions or just the simple jokes of the day. So to all of you a big thanks and I hope you all continued success here at Baylor and wherever you go after graduation. I would finally like to thank my fiancé Morgan. She is a true blessing to have and has been ever so supportive over the past two years. Her words have help guide me and made even the most frustrating of days bearable.

CHAPTER ONE

Introduction

The main motivation for my thesis was to determine the strength and orientation of seismically anisotropic fabrics beneath Texas and Oklahoma, identify the relationship between seismic anisotropy and geologic features of the area and finally to infer the main geophysical causes for the seismic anisotropy. None of this would have happened without first the help of my co-author Dr. Jay Pulliam, and the introduction of the EarthScope program to Texas and Oklahoma in early 2009. Very little is known about the deep Earth structure of the region due to the lack of seismic instrumentation as it pertains to deep Earth seismology. This thesis, which has been formatted in the American Geophysical Union format style, illustrates that, in Texas and Oklahoma, shear wave splitting results show that the fast axis directions are parallel to sub-parallel to the average plate motion of the North American plate. When taking a closer look at the results we see that along the Gulf coast delay times range upwards of 2.0 s and reveal considerable contribution from the mantle. On the stable craton delay times range from 0.9 s to less than 0.5 s. These results indicate that the major contribution of anisotropy is most likely due to shearing forces as the lithosphere moves over the underlying asthenosphere. Along the Southern Oklahoma Aulacogen (SOA) fast axis directions are parallel to the rift of the Aulacogen. This is consistent with a shape preferred orientation anisotropy. This thesis along with others currently ongoing at Baylor will hopefully unravel key information about the deep Earth geology of both Texas and the gulf coast plain.

CHAPTER TWO

Manuscript One

Seismic Anisotropy in Texas and Oklahoma and its relationship to tectonic events that shaped southern Laurentia

Abstract. We present new shear wave splitting measurements of approximately 1500 SKS phases recorded at 176 transportable array and permanent broadband seismic stations deployed in Texas and Oklahoma. Measurements of SKS splitting on the North American craton show NE-SW fast axis polarization directions that are generally parallel to subparallel to the absolute motion of the North American plate. In the vicinity of the Southern Oklahoma Aulacogen the fast axis polarization direction changes to NW-SE and parallels the strike of the Aulacogen. Along the continental-oceanic transition zone (COTZ), SKS phases show a NE-SW fast axis polarization and are consistent with the motion of the North American plate. However, large delay times, approaching 2.3s, are observed on the COTZ, compared to delay times of less than 1.5s observed on the craton. An analysis that uses the geographic distribution of measurements to estimate the depth to the anisotropic layer indicates the depth beneath the craton is approximately 180 km and 280 km for the COTZ. Observed patterns of fast axis directions parallel to plate motions, small delay times, and a shallower depth to the anisotropic zone are consistent with a lithospheric origin for the observed anisotropy on the craton. Larger delay times and a deeper anisotropic source suggest that asthenospheric flow around the keel of the North American craton is responsible for the seismic anisotropy observed along the transition zone.

1. Introduction

For over 30 years, shear wave splitting measurements have been used to infer the existence of mantle fabrics and to characterize their strength and orientation beneath continents and oceans, actively-deforming as well as stable continental regions, subduction zones, and mid-ocean spreading centers [e.g., *Silver and Savage*, 1994; *Wolfe and Silver*, 1998; *Savage*, 1999; *Gao and Liu*, 2012]. Stable continental interiors contain the Earth's oldest lithosphere and have accumulated a long record of tectonic events, so the study of anisotropic structure can reveal a great deal about those events [*Fouch and Rondenay*, 2006]. Most of Texas and Oklahoma are part of the approximately 1.4 bya Laurentia craton [*Hoffman*, 1988; *Harry and Londono*, 2004] that extends from Texas to Canada, where it is exposed as the Canadian Shield. During this large time span, orogenic and rifting processes have deformed and reworked the craton. The Grenville orogeny 1.1 bya [*Mosher et al*., 2008] led to the formation of the supercontinent Rodinia while the Ouachita orogeny 300 mya [*Stern et al*., 2010] led to the formation of Pangea. These supercontinents were broken up by rifting events in the Cambrian (530 mya), giving rise to the Rheic ocean [*Thomas*, 2006], and again in the Jurassic (165 mya), resulting in the opening of the Gulf of Mexico (GoM) [*Stern et al*., 2010]. These episodes of deformation formed the main geological features of the region, including Precambrian exposures of the Llano uplift in central Texas, the Ouachita Deformation Front (ODF) that extends from southern Texas to the Wichita Mountains of southern Oklahoma, and the Southern Oklahoma Aulacogen (SOA).

While stable continental interiors harbor the longest record of tectonic deformation, the greatest tectonic activity, and therefore deformation, typically occurs at the margins of continents. Yet, patterns of mantle deformation beneath regions in which continental lithosphere transitions to oceanic lithosphere are still poorly documented and poorly understood. In the case of the Gulf Coast region of the United States, this is because lithosphere that was formed or deformed by tectonic events has subsequently been covered by millions of years of sedimentary successions [*Harry and Londono*, 2004] and because there have been relatively few broadband seismographs located in this region due to its relatively low seismic hazard. As a result, little is known about the deep structure at the margins of southern Laurentia and the continent-oceanic transition zone (COTZ).

Tools such as the broadband seismographs that recently traversed the region as part of the EarthScope program allow us to learn a great deal about the structure of the region's crust and upper mantle and, by inference, its geologic history. Seismic anisotropy may result from the alignment of inherently anisotropic minerals, caused by "flow" or deformation, or from the creation of fabrics in otherwise isotropic materials [*Silver and Chan*, 1991, *Silver and Savage*, 1994]. Measuring seismic anisotropy over a broad region can allow us to unravel the region's deformation history and tectonic past. Teleseismic events (XKS, including SKS, SKKS and PKS) have been used widely to infer the existence, orientation, and strength of seismic anisotropy [*Silver and Savage*, 1994; *Savage*, 1999]. XKS phases are most commonly used for these measurements because their particle motion becomes polarized in the SV (vertical) direction upon their conversion from P to S-waves (denoted by "K" in SKS) as they re-enter the mantle at the

core-mantle boundary (CMB), so that their original polarization characteristics are erased [*Savage*, 1999]. In a purely homogeneous and isotropic Earth, an SKS phase would only register motion in the radial direction on a three-component seismograph (once the seismograph's original components are digitally rotated into the appropriate radial-transverse-vertical coordinate system). A record of energy on a station's transverse component is therefore a diagnostic feature of seismic anisotropy. If a "split" shear wave is observed at a station, meaning that energy appears on both the radial and transverse components of the seismograph, we can assume that at some time along the path from the CMB to the station the shear wave encountered an anisotropic medium [*Silver*, 1996; *Savage,* 1999]. Measurements can then be made of the shear wave's split in order to characterize the strength and orientation of seismic anisotropy sampled by the wave. The difference between arrival times of the resolved shear wave is known as the "delay time" (δt). The fast shear wave polarization direction (ϕ) describes the orientation of the anisotropic medium.

Long et al. [2009] argues that the main cause of seismic anisotropy is the preferred orientation of upper mantle minerals; olivine $(Mg,Fe)_2SiO_4$ is the most common upper mantle mineral [*Hannah and Long, 2012*]. As olivine undergoes shearing it develops a lattice-preferred orientation (LPO) and becomes anisotropic in the direction of flow on length scales applicable to characteristic seismic wave propagation in the mantle [*Hanna and Long*, 2012]. For a simple case of mantle flow, the fast shear wave propagation direction will correspond to the maximum shear direction for large strains (i.e. the direction of mantle flow beneath a seismic station [*Zhang and Karato*, 1995]. This "A-type" olivine is usually the result of shearing forces as the upper lithosphere

moves over the underlying, more ductile asthenosphere [*Silver*, 1996]. We do note the study by *Jung and Karato* [2001] that states in the presence of a substantial amount of water, how some olivine minerals tend to deform perpendicular to the maximum shear direction. This type of olivine is called a "B-type" olivine and can be used to explain the trench parallel fast axis directions along subducting slabs [*Jung and Karato,* 2001]. For the interpretation of shear wave splitting measurements, the only type of olivine that alters the relationship between flow and fast axis direction is B-type. A-type olivine is thought to make up a majority of the olivine in the mantle while the B-type is thought to be restricted to some forearc corners of subduction zone mantle wedges [*Long and Silver,* 2009]. Other causes of seismic anisotropy include shape-preferred orientations (SPO) and structural or fossil anisotropy. SPO occurs when pockets of partial melt align, causing seismic anisotropy that is not directly related to mantle flow [*Zimmerman et al*., 1999; *Fouch and Rondenay*, 2006]. The fast polarization direction occurs along the long axis of structures such as tubes or lenses. Evidence suggests that SPO plays an important role in the development of seismic anisotropy in active continental rift zones [*Barruol and Hoffman*, 1999; *Fouch and Rondenay*, 2006] but studies that would elucidate their contribution to seismic anisotropy beneath passive margins have not been performed. Fossil anisotropy reflects the remains of past tectonic events "frozen" in the upper part of the crust that was deformed though orogenic or extensive processes [*Barruol and Hoffman*, 1999; *Walker et al*., 2004]. These past tectonic events, although no longer active, can still influence seismic anisotropy in the upper crust.

Fouch et al. [2000] and *Fouch and Rondenay* [2006] show that sources of seismic anisotropy beneath stable continental interiors are a combination of lithospheric and

sublithospheric fabrics, which are remnants of prior tectonic activity on the continent. *Fouch and Rondenay* [2006] note that under the Australian craton, a strong relationship exists between APM and fast axis polarizations, mainly due to the high rate of motion of the Indo-Australian plate, but can find only regional relationships between APM and fast axis polarizations under slower-moving continents, such as North America. *Assumpção et al*. [2011] describes a regional relationship between APM and fast axis directions under the South American craton but suggests that an observed change in fast axis directions may be due to a diversion of mantle flow around a deep keel underneath the South American craton and to a larger component of lithospheric or fossil anisotropy due to the thickness of the craton.

In Texas and Oklahoma, however, there have been only sparse measurements of seismic anisotropy parameters, mainly due to a dearth of broadband seismic stations. Texas and Oklahoma are prolific producers of oil and natural gas. Therefore, most seismic investigations have targeted the region's sedimentary basins with seismic reflection surveys for purposes of petroleum exploration [*Mickus et al*., 2009]. While modern seismic reflection methods may include analyses of anisotropy in the subsurface, exploration-oriented studies are sensitive to only the top few kilometers of the Earth. Studies of the upper mantle, for example, require larger energy sources and, therefore, different types of recording instruments and analysis techniques.

Previous studies of Texas and Oklahoma reveal three distinct provinces based upon seismic anisotropy characteristics, as shown in Figure 1: 1) A cratonic province that covers most of the region, 2) the Southern Oklahoma Aulacogen, which lies within the cratonic area and is characterized by a large, positive gravity anomaly, and 3) a continent-

ocean transition zone that extends southward and eastward from the Ouachita Deformation Front to the Texas Gulf Coast [*Pulliam and Sen* [1998], *Gao et al.* [2008] and *Satsukawa et al*. [2010]]. *Pulliam and Sen* [1998] and *Gao et al*. [2008] reveal that stations located on the North American craton exhibit small delay times and fast polarization directions that generally parallel the strike of local crustal geological features and attributed the anisotropy on the craton to lithospheric deformation. *Gao et al*. [2008] also point out that their measurements of ϕ and δt in the vicinity of the SOA are similar to those observed at active continental rift zones. In each of these cases, the fast axis of polarization is parallel to the axis of the rift [*Gao et al*., 1997]. Along the Gulf Coast, SKS results measured by *Gao et al*. [2008] and *Pulliam and Sen* [1998] exhibit large delay times (>1.5 s) and fast polarization directions parallel to the average direction of motion of the North American Plate. *Gao et al*. [2008] attribute the seismic anisotropy observed in this region to either asthenospheric flow below the thinned lithosphere of the continent-ocean transition, magma-filled cracks, or a combination of the two. *Satsukawa et al*. [2010] propose that the large variation in delay times over tens of kilometers laterally on the Llano uplift imply a relatively shallow, i.e., lithospheric, source of anisotropy.

All of the previous studies of SKS splitting in Texas and Oklahoma were based upon measurements at only a few stations, which sample the region only sparsely. With the arrival of EarthScope's Transportable Array (TA) in 2008 it became possible to conduct a study of SKS splitting characteristics much more densely, resulting in higher resolution (on average), and comprehensively. The nominal spacing of EarthScope TA stations is 70 km, which compares favorably to the sensitivity of splitting parameters in

the mantle. We also include measurements from a temporary, approximately linear deployment of broadband stations across the Gulf Coastal Plain. The average station spacing along the transect is 17 km. Measurements of SKS splitting at these stations promises a more complete picture of seismic anisotropy beneath Texas and Oklahoma and offers hope for more definitive conclusions regarding the causes of seismic anisotropy. Because this region comprises a transition from a continental craton to transitional crust and, ultimately, to true oceanic crust in the Gulf of Mexico and has been the site of significant alteration by plate tectonic events, lessons learned about the nature of the lithosphere and asthenosphere across this transition will inform our understanding of such transitions elsewhere.

2. Methods

We used the program *SplitLab* to measure parameters that describe seismic anisotropy [*Wüstefeld et al*., 2008]. *SplitLab,* which runs inside the Matlab® environment, has been used in numerous shear wave splitting studies [e.g., *Long et a*l., 2009; *Bonnin et al*., 2010; *Satsukawa et al*., 2010; *Assumpção et al*., 2011; *Hannah and Long*, 2012; *Meighan and Pulliam*, 2012] and has proven to be a robust measurement tool. *SplitLab* (Figure 2) provides a graphical user interface (GUI) that streamlines the estimation of SKS splitting parameters. SplitLab associates earthquake waveform files in SAC format (Seismic Analysis Code) [*Goldstein et al*., 1998, 2003] to events listed in the Global CMT catalog [*Ekström et al.*, 2012] and then allows the user to visually inspect and analyze each seismogram. After the seismogram has been rotated to a great-circle path between the seismographic station and the earthquake, the user can apply filters to

increase the signal to noise ratio. The user manually chooses the time window and SplitLab then automatically performs splitting measurements via three techniques: 1) the minimum energy method (SC) [*Silver and Chan*, 1991], 2) the eigenvalue method (EV) [*Silver and Chan*, 1991], and 3) the rotation-correlation method (RC) [*Bowman and Ando*, 1987]. All three methods conduct a grid search to determine the best splitting parameters (ϕ and δt), as shown in Figure 2. Following *Growdon et al*. [2009] we apply the following criteria to ensure that our splitting measurements are robust and reliable: 1) the particle motion that corresponds to the arrival of split SKS waves must be elliptical before and linear after correction, 2) the grid search method must show a well-defined minimum, 3) the fast axis must not be parallel or perpendicular to the great-circle path that connects the station to the earthquake (i.e., to the station-event backazimuth), 4) the time window used must be equal to or greater than 10 s and, 5) the RC and SC methods must agree, within reasonable bounds.

To minimize noise we stacked the error surfaces computed via grid searches for individual station-event pairs at a given station and found the final estimates of ϕ and δt via a grid search of the stacked surface [*Monteiller and Chevrot*, 2010]. This approach yields one stacked ϕ and δt measurement per station as well as an estimate of uncertainty for each measurement. Stacking the final results in conjunction with the qualifying criteria described above allows us to produce a quantitative measure of confidence in the accuracy of our splitting measurements.

2.1 AnisDep

To estimate the depth to anisotropy in the study area, the Fortran program AnisDep [*Gao and Liu*, 2012] was used. This program estimates the likely depth to the anisotropic layer by evaluating quantitatively the spatial coherency of teleseismic shear-wave splitting parameters. Due to the steep incidence of SKS raypaths, analyses of shear-wave splitting that rely on measurements at individual stations offer good lateral resolution but poor vertical resolution [*Liu and Gao,* 2011]. *Gao and Liu* [2012] demonstrate that, by examining the coherency of splitting patterns at a set of closely spaced stations, one can estimate depth dependence of seismic anisotropy, to first order.

To apply AnisDep, the study area is first divided into square 1° blocks. Each of these blocks is weighted with a variation factor, F_v, which is the weighted sum of the standard deviation for the observed splitting measurements over all blocks. The geographic coordinates of ray piercing points are then calculated for the top of each layer. For each depth layer, a total F_v for all blocks is computed, along with its standard deviation. The "optimal depth" is indicated by the minimum value of F_v, which corresponds to the "minimum variation" depth, or the depth that produces the greatest coherency between measurements at adjacent stations, and corresponds to the depth of a layer of anisotropy [*Gao and Liu,* 2012]. Using the AnisDep program in conjunction with our dataset we were able to estimate depths to the anisotropic zone beneath two regions within our study area and assess variations of these depths in the context of other geophysical observables, as well as surface features.

3. Data

We requested three-component, teleseismic SKS and SKKS waveform data for the years 2009-2012 from the IRIS Data Management Center for a total of 176 broadband stations. Of these 176, 153 stations belong to EarthScope's Transportable Array, four are permanent stations maintained by the U.S. Geological Survey, and 19 were deployed by Baylor and Texas Tech Universities. These latter 19 stations were deployed in a transect that extends from Johnson City, Texas, which lies on the stable North American craton, to Matagorda Island, on Texas' Gulf Coast. The seismographs consisted of Reftek 130 digitizer/recorders and a combination of Guralp 3T, Guralp 3ESP, and Nanometrics Trillium Compact seismometers, all with flat responses between 120 s (0.00833 Hz) and 50 Hz.

We visually examined approximately 14,000 teleseismic SKS and SKKS events recorded at our stations with distances ranging from 90° to 130° from earthquake hypocenters of magnitude 5.5 or greater. Using the previously stated criteria for splitting we made measurements of ϕ and δt for all clear SKS arrivals and a smaller set of SKKS arrivals for each station-earthquake pair. SKKS signals were measured, in most cases, when the number of SKS measurements was meager.

Of the approximately 14,000 SKS and SKKS events viewed, about 1500 passed the qualifying criteria. Figure 3 shows the typical distribution of measureable earthquake events for the study region. The majority of events were scattered along the Philippian and Tongan subduction zones with a large number of backazimuths between 180°-330° while the largest gap between a significant number of events exists between 60° and 150°. This gap in seismic events is due mainly to the lack of seismic activity in the region

associated with the stable African craton. The events measured had focal depths of less than 100 km and magnitudes between 5.5 and 7.0.

4. Results

We divided our study area into three distinct regions based upon tectonic and structural features at the Earth's surface (Figure 1). The first region (Region I) encompasses a portion of the North American craton that stretches from the Ouachita Deformation Front northward. One hundred and one TA and permanent stations were deployed on the craton. Region II extends from southwestern Oklahoma into the panhandle of Texas and is characterized by a high gravity anomaly. This region is associated with the Southern Oklahoma Aulacogen [*Barruol et al*., 1997]; our measurements within the Aulacogen came from 10 stations. Region III encompasses the Gulf Coast Plain and the Continent-Ocean Transition Zone. Our measurements within this sub-region came from 65 stations located along the Gulf Coast area to the south and east of the ODF. As shown in Figure 4 and Table 1 of the supplemental materials, the 176 broadband seismic stations provided delay times ranging from 0.25-2.3 s and fast polarization directions ranging from 14°-345° measured clockwise from north. Shear wave splitting measurement errors are plotted using a 95% confidence interval [*Silver and Chan*, 1991; *Fouch et al*., 2000; *Wang et al*., 2008]. The conservative error bounds shown in Figure 5 were determined by the minimum and maximum of the 95% confidence region [*Wüstefeld et al*., 2008].

4.1. North American Craton

Region I is generally characterized by an NE-SW fast axis polarization direction. Delay times range between 0.30-1.55 s with the smaller delay times measured on the Llano uplift and larger delay times measured north of the SOA. Errors in region I vary ± 10-15° from the average fast axis direction and ± 0.15 s from the average δt measurement.

4.2. Southern Oklahoma Aulacogen

Region II is characterized by a NW-SE fast axis polarization direction, which is consistent with the sole previous measurement in this region [*Gao et al*., 2008], and delay times between 0.40-1.60 s, with smaller delay times on the western terminus of the Aulacogen and larger delay times near the ODF. Errors along the Aulacogen are consistent, with the exception of the western terminus of the Aulacogen, where ϕ has an error of ± 25°.

4.3. Continental-Oceanic Transition Zone (COTZ)

Region III is characterized by an ENE-SSW fast axis polarization direction and larger delay times, ranging from 0.85-2.05 s (± .25-.35 s). Along the Baylor/Texas Tech transect, ϕ is consistent with both the surrounding TA stations and previous studies. We also see a gradual increase of delay times from 0.85 s at the northern end of the line to 2.05 s at the GoM, the line's southern terminus.

The splitting parameters (ϕ and δt) determined by SplitLab, before stacking, were input to AnisDep [*Gao and Liu*, 2012] in order to estimate the likely depth for the source

of seismic anisotropy. Data from regions I and II were combined to obtain a depth for anisotropy beneath the broad North American craton and data from region III were used to estimate the depth to an anisotropic layer beneath the passive margin. AnisDep yielded results for a layer of anisotropy approximately 180 km beneath the craton (Figure 6a) and 280 km beneath the transition zone (Figure 6b).

5. Discussion

The orientations of fast axis polarization directions are consistent with the average plate motion of the North American plate as calculated by the MORVEl no-net rotation (NNR) model [*DeMets et al*., 2010] (Figure 4). The EarthScope Automated Receiver Survey (EARS) [*Crotwell and Owens*, 2005] yielded crustal thicknesses for the craton on the range of 42-46 km (Figure 7), with the thickest crust located beneath the Llano uplift. The automated EARS values are subject to error but they represent the only comprehensive set of crustal thickness estimates available. These results yield reasonable, although slightly thicker, estimates compared to the 41-km global average for continental crust [*Christensen and Mooney*, 1995]. These results, along with the estimated 180 km deep source of seismic anisotropy, are consistent both with upper mantle lithospheric anisotropy and with previous studies of seismic anisotropy beneath stable cratons [*Fouch et al*., 2000; *Fouch and Rondenay*, 2006; *Gao et al*., 2008; *Asumpçao et al*., 2011]. The depth estimate of 180 km to the anisotropic zone and the small delay times found on the craton, relative to the global average of 1.0 s [*Silver*, 1996], point to the possibility that anisotropy arises as a result of shearing as the North American lithosphere moves over the underlying asthenosphere. The small perturbations in both ϕ and δt on the craton can

be attributed to variations in shearing, perhaps corresponding to variations in lithospheric thickness, or to second-order anisotropy located in the lithosphere itself, called "frozen anisotropy" by some authors [*Savage*, 1999; *Fouch and Rondenay*, 2006; *Wang et al*., 2008]. "Frozen anisotropy" is associated with past deformation (tectonic) events. Variations are particularly large at stations located on and around the Llano uplift, where delay times are on the order of 0.3-0.5 s, well below the global crustal average of 1.0 s. A study by *Simons and van der Hilst* [2003] measured split times on the Precambrian terranes of Australia to be 0.3-0.6 s, comparable to our observations for the Llano uplift. Seismic anisotropy for that region was attributed to the influence of older crustal deformation features (fossil anisotropy), which accounted for the small delay times.

Another reason for such small delay times on the Llano uplift could be a cancelling of delay times due to multiple shallow and weaker layers of anisotropy confined in the crust that exhibit fast directions orthogonal to the deeper lithospheric anisotropy [*Gao et al*., 2008]. We do note that many previous tectonic events are generally oriented in the direction of current plate motion. In some cases this can make it difficult to distinguish between plate motion effects on seismic anisotropy and tectonic effects, but the results from AnisDep help identify the two contributions.

The NW-SE orientation of the fast axis directions at the stations located within the SOA is similar to orientations observed by other authors at active rifts, such as the Rio Grande Rift [*Sandvol et al*., 1992] and the East Africa Rift [*Gao et al*., 1997; 2005]. The fast axis polarization direction for the SOA is roughly parallel to the axis of the rift and follows the large gravity anomaly (Figure 8) that outlines the SOA. The large range of fast axis directions is most likely due to the transition between tectonic provinces,

from a tectonic regime dominated by the Aulacogen to a craton-dominated regime in the panhandle of Texas, which is believed to be the western terminus of the SOA [*Hogan and Gilbert*, 1998; *Barruol et al*., 1997]. Given the AnisDep result, the anisotropy found here is concentrated in the lithosphere and is likely caused by the velocity contrasts of the lower shear wave velocity of the NW-striking magmatic dikes and lenses that formed during the Paleozoic [*Thomas*, 2006] to the higher velocity rocks surrounding the dikes [*Lin et al*., 1994]. Also, surface geological and geophysical data suggest that an approximately 10-km-thick mafic-layered complex lies beneath the SOA, which helps explain the large gravity anomaly associated with the Aulacogen [*Hogan and Gilbert*, 1998] (Figure 8).

The large gradient of delay times associated with stations from the Ouachita Deformation Front south to the Gulf Coast Plain are much larger than the 1.0 s global average. Split times larger than 1.0 s generally require significant seismic anisotropy in the mantle, because the waves' relatively short path lengths in the crust do not allow the waves to accumulate such large time delays [*Savage*, 1999; *Growdon et al*., 2009]. The crustal thickness of the COTZ varies from 28-36 km, as reported by EARS (Figure 7). The thinning of the crust is attributed to two stages of rifting during the Cambrian (540 Ma) and again during the Jurassic (165 Ma) [*Thomas*, 2006]. Using AnisDep, we were able to obtain a depth to anisotropy of approximately 280 km, a significantly greater depth than was found for the craton. This deeper depth is likely to occur in the asthenosphere, which is generally believed to be thicker than the lithosphere. Experiencing a thicker layer of anisotropy allows SKS waves to accumulate larger delay times [*Savage*, 1999; *Grodwon et al*., 2008; *Wang et al*., 2008]. The COTZ stations

exhibit the largest delay times in the entire TX/OK region and supports the scenario in which anisotropy derives from the asthenosphere. Because of the orientation of the fast axis polarization direction with respect to the APM of the North American plate and the large delay times, a likely cause of the formation of seismic anisotropy in the continental-oceanic transition zone is present-day asthenospheric flow around the keel of the North American craton (Figure 9). This model is consistent with results of a recent joint inversion of surface waveforms and shear-wave splitting results by *Fouch et al*. [2000]. For stations located on the eastern North American craton, fast axis directions that are roughly parallel to the APM of the North American plate, while the easternmost stations showed variations in fast axis directions and splitting times on the order of 1.0 s. *Fouch et al.* [2000] argue that the anisotropy in continental/transitional settings is derived from both continental lithosphere and asthenospheric flow around the keel of the North American craton.

6. Conclusions

The goal of this study was to identify and measure seismic anisotropy in Texas and Oklahoma through shear wave splitting measurements. This region marks the first arrival by the EarthScope's Transportable Array at a "passive margin", a boundary that is not undergoing differential motion at present. The seismic reconnaissance of the region by the Transportable Array provides observations that are unprecedented in density and number. These data allow us to estimate, for the first time in this region, splitting parameters on a scale that (a) can be interpreted meaningfully in terms of tectonic structures and (b) can be analyzed for coherency to estimate depths to anisotropic layers.

The results presented here illustrate significant variations and patterns of shear wave splitting parameters in the region. These variations can be linked to both structures produced by known tectonic events in the region's history and to likely depths to anisotropic layers that support proposed links between shear wave splitting, tectonic structures, and mantle deformation. Beneath the cratonic stations, observed shear-wave splitting measurements and depth estimates suggest seismic anisotropy in the lithospheric mantle. This can be attributed to shearing as the thick North American lithosphere overrides the underlying asthenosphere, causing fast axis polarization directions to be consistent with the APM of the North American plate. Also, second-order shallow "frozen" lithospheric anisotropy, due to deformation from past tectonic events, explains the variations of delay times associated with the Llano Uplift. Beneath the SOA, where our depth estimate to anisotropic material is significantly less deep (180 km) than beneath the stretched and thinned transitional crust of the Gulf Coastal Plain (280 km), we argue that lithospheric anisotropy in the form of rift-parallel dikes is the main cause of seismic anisotropy. Surface geological and geophysical data have found rift-parallel dikes to be a main contributor to seismic anisotropy in rifted areas [*Gao et al.,* 1997]. Beneath the COTZ stations, delay times are greater and fast axis polarization directions remain consistent with the APM of the North American plate. The increase of delay times is most likely due to the thinning of the crust along the transition zone (as supported by the EARS receiver function data), resulting in a thinner crust and lithosphere and a thicker asthenosphere. In this scenario, delay times are greater than those beneath the craton because the lithosphere has been thinned by the 165 Ma rifting event that created the Gulf of Mexico. A thinner lithosphere results in longer path lengths of XKS waves through an

asthenosphere in which highly anisotropic olivine minerals have been aligned by mantle flow. We therefore conclude that anisotropy in the COTZ region is due to asthenospheric flow around the keel of the North American craton. Mirroring events at the Earth's surface, the cratonic keel is likely to have become undulated during previous tectonic events that deformed the region extensively. Most prominent among these events is the Ouachita Orogeny, which is believed to have occurred 300 mya [*Stern et al*., 2010].

7. Acknowledgements

We thank the EarthScope Program and the Incorporated Research Institutions for Seismology (IRIS) for their roles in acquiring, archiving, and disseminating broadband seismic data on an unprecedented scale in Texas and Oklahoma. We thank A. Wüstefeld for access to his SplitLab software, H. Gurrola and students of Baylor and Texas Tech Universities for their efforts to acquire broadband data from a transect across the Texas Gulf Coastal Plain. Funding is gratefully acknowledged from the National Science Foundation (EAR 0746321), the Norman Hackerman Advanced Research Program (Award # 003658-0034-2009), the Gulf Coast Association of Geological Societies, and the W.M. Keck Foundation

References

Asumpçao, M., M. Guarido, S. van der Lee, S.C. Dourado (2011), Upper-mantle seismic anisotropy from SKS splitting in the South American stable platform: A test of asthenospheric flow models beneath the lithosphere, Lithosphere, 3, 173-180, doi: 10.1130/L99.1

Barruol, G., P. G. Silver, and A. Vauchez (1997), Seismic anisotropy in the eastern United States: Deep structure of a complex continental plate, *J. Geophys. Res.*, *102*(B4) 8329–8348, doi:10.1029/96JB03800.

Barruol, G., and R. Hoffman (1999), Upper mantle anisotropy beneath the Geoscope stations, J. Geophys. Res., 104, 10,757–10,773.

Bonnin, M**., G.** Barruol, and G.H.R. Bokelmann, (2010), Upper Mantle Deformation beneath the North American-Pacific Plate Boundary in California from SKS splitting,J. Geophys. Res, 115, B04306, doi:10.1029/2009JB006438.

Bowman, J.R., and M. Ando (1987), Shear-wave splitting in the upper-mantle wedge above the Tonga subduction zone. Journal of Royal Astronomical Society, 88, 25-41

Christensen, N. I., and W. D. Mooney (1995), Seismic velocity structure and composition of the continental crust: A global view, J. Geophys. Res., 100(B6), 9761–9788, doi:10.1029/95JB00259

Crotwell H. P., T.J. Owens (2005), Automated Receiver Function Processing, Seism. Res. Lett., 76, 702-709. doi: 10.1785/ gssrl.76.6.702

DeMets, C., R.G.Gordon, and D.F. Argus (2010), Geologically current plate motions, Geophysical Journal International, v. 181, no. 1, p. 1-80, doi: 10.1111/j.1365-246X.2009.04491.

Ekström, G., M. Nettles, and A.M. Dziewoński (2012). The global CMT project 2004 2010: Centroid-moment tensors for 13,017 earthquakes. Phys. Earth Planet Int., 200 201,1–9.

Fouch, M.J., T.J. Clarke, K.M. Fischer, E.M. Parmentier and M.E. Wysession (2000), Shear-wave splitting, continental keels, and patterns of mantle flow: Journal of Geophysical Research, B: Solid Earth, V. 105, p. 6255-6275, doi: 10.1029/1999JB900372.

Fouch, M.J., and S.Rondenay (2006), Seismic anisotropy beneath stable continental interiors. Phys. Earth Planet. Inter. 158, 292–320. doi: 10.1016/J.pepi.2006.03.024

Gao, S., P.M. David, H. Liu, P.D. Slack, A. W. Rigor, Y.A. Zorin, V.V. Mordvinova, V.M. Kozhevnikov, and N.A. Logatchev (1997), SKS splitting beneath continental rift zones: Journal of Geophysical Research, v. 102 pp. 22781-22797, doi:10.1029/97JB01858.

Gao, S. S., K. H. Liu, R. J. Stern, G. R. Keller, J. P. Hogan, J. Pulliam, and E. Y. Anthony (2008), Characteristics of mantle fabrics beneath the south-central United States: Constraints from shear-wave splitting measurements, Geosphere, 4, 411 – 417, doi:10.1130/GES00159.1.

Gao, S.S. and K.H. Liu (2012), AnisDep: A FORTRAN program fro the estimation of the depth of anisotropy using spatial coherency of shear-wave splitting parameters. Computers and Geosciences, doi: 10.1016/j.caego.2012.01.020.

Goldstein, P., D. Dodge, M. Firpo, S. Ruppert (1998) "What's new in SAC2000? Enhanced Processing and Database Access", Invited contribution in Seismological Research Letters, 69, 202-205, 1998

Goldstein, P., D. Dodge, M. Firpo, Lee Minner (2003) “SAC2000: Signal processing and analysis tools for seismologists and engineers, Invited contribution to “The IASPEI International Handbook of Earthquake and Engineering Seismology”, Edited by WHK Lee, H. Kanamori, P.C. Jennings, and C. Kisslinger, Academic Press, London.

Growdon M.A., G.L. Pavlis, F. Niu, F.L. Vernon, and H. Rendon, (2009), Constraints on mantle flow at the Caribbean-South American plate boundary inferred from shear wave splitting. *Journal of Geophysical Research*, 114, B02303.

Hanna M.D. Long (2012), SKS splitting beneath Alaska: Regional variability and implications for subduction processes at a slab edge, Tectonophysics, Volumes 530–531, Pages 272-285, ISSN 0040-1951. 10.1016/j.tecto.2012.01.003.

Harry, D. L., and J. Londono (2004), *Bulletin of the Geological Society of America* 116, 188-199. doi: 10.1130/B25237.1

Hoffman, P.F. (1988), United plates of America, the birth of a craton: Early Proterozoic assembly and growth of Laurentia: Annual Review of Earth and Planetary Sciences, V. 16, p. 543-603. doi: 10.1146/annurev. ea.16.050188.002551.

Hogan, J.P., and M.C. Gilbert (1998), The southern Oklahoma Aulacogen, *in* Olsen, K.H., ed., Continental rifts: Evolution, structure and tectonics: Developments in | Geotectonics Volume 25: Amsterdam, Elsevier, p. 427-436.

Jung H., and S. Karato (2001), Water-induced fabric transitions in olivine. Science 293:1460 1463

Liu, K.H., and S.S. Gao (2011), Estimation of the depth of anisotropy using spatial coherency of shear-wave splitting parameters, Bulletin of the Seismological Society of America 101 (5), doi: 10.1785/0120100258.

Long, M.D., and P.G. Silver (2009), Shear wave splitting and mantle anisotropy: measurements, interpretations, and new directions. Surv. Geophys. 30, 407–461.

Long, M.D., H.G. Gao, A. Klaus, L.S. Wagner, M.J. Fouch, D.E. James, and E.Humphreys (2009), Shear wave splitting and the pattern of mantle flow beneath eastern Oregon Earth Planet. Sci. Lett., 288 pp. 359–369,doi10.1016/j.epsl.2009.09.039

Meighan, H. E., and J. Pulliam (2012), Seismic anisotropy beneath the Northeastern Caribbean: Implications for the subducting North American lithosphere, in *Caribbean Geosciences, Bulletin de la Société Géologique de France, Special Issue*, edited by O. Lacombe, J.F. Lebrun and B. Marcaillou, in press.

Mickus, K. R., J. Stern, G.R. Keller, and Y.E. Anthony (2009), Potential field evidence for a volcanic rifted margin along the Texas Gulf Coast, *Geology, 37*, 387-390. doi: 10.1130/GES00532.1

Monteiller V., and S. Chevrot (2010), How to make robust splitting measurements for single-station analysis and three-dimensional imaging for seismic anisotropy. *Geophysical Journal International*, 182, 311-328. doi: 10.1111/j.1365-246X.2010.04608.x

Mosher, S., J.S. Levine, and W.D. Carlson, (2008), Mesoproterozoic plate tectonics: A collisional model for the grenville-aged orogenic belt in the Llano Uplift, central Texas. *Geology* 36 (1), 55–58. doi: 10.1130/G24049A.1

Pulliam, J. and M.K. Sen (1998), Seismic anisotropy in the core–mantle transition zone. Geophysical Journal International, 135: 113–128. doi: 10.1046/j.1365-246X.1998.00612.

Sandvol, E., J. Ni, S. Ozalaybey, and J. Schlue (1992), Shear-wave splitting in the Rio Grande Rift: Geophysical Research Letters, v. 19, p. 2337-2340. doi: 10.1029/92GL02715

Satsukawa, T., K. Michibayashi, E.Y. Anthony, R.J. Stern, S.S. Gao and K.H. Liu, (2011), Seismic anisotropy of the uppermost mantle beneath the Rio Grande rift: Evidence from Kilbourne Hole peridotite xenoliths, New Mexico. *Earth and Planetary Science Letters*, 311(1-2), 172-181,doi:10.1016/j.epsl.2011.09.013

Savage, M.K. (1999), Seismic anisotropy and mantle deformations: What have we learned from shear wave splitting? Reviews of Geophysics v. 37, p. 65-106 doi:10.1029/98RG02075.

Silver, P.G. (1996), Seismic anisotropy beneath the continents: Probing the depths of geology, *Annual Rev. Earth and Planet. Sci*., 24, 385-432, doi: 10.1146/annurev.earth.24.1.385.

Silver, P.G., and W. Chan (1991), Shear wave splitting and subcontinental mantle deformation. Journal of Geophysical Research 96, 16429-16454.

Silver, P. G. and M.K. Savage (1994), The Interpretation of Shear-Wave Splitting Parameters In the Presence of Two Anisotropic Layers. Geophysical Journal International, 119: 949–963. doi: 10.1111/j.1365-246X.1994.tb04027.

Simons, F. J., and R.D van der Hilst (2003), Seismic and mechanical anisotropy and the past and present deformation of the Australian lithosphere. Earth Planet. Sci. Lett. 211, 271–286, doi: 10.1016/S0012-821X(03)00198-5.

Thomas, W. A. (2006), Tectonic inheritance at a continental margin, GSA Today, 16, 4-11, doi: 10.1130/1052-5173(2006)016[4:TIAACM]2.0 CO;2.

Stern, R., W.R. Dickinson, and T. Lawton, (2010), Introduction: Making the Southern Margin of Laurentia. *Geosphere:* v: 6; no. 6; p. 737-738; doi: 10.1130/GES00642.1

Walker, K.T., A.A. Nyblade, S.L Klemperer, G.H.R. Bokelmann, and T.J.Owens (2004), On the relationship between extension and anisotropy: constraints from shear-wave splitting across the East African Plateau. J. Geophys. Res. 109 (B8), B08302.

Wang, X., J.F. Ni, R. Aster, E. Sandvol, D. Wilson, C. Sine, S.P. Grand, and S. Baldridge (2008), Shear-wave splitting and mantle flow beneath the Colorado Plateau and its boundary with the Great Basin: Bulletin of the Seismological Society of America, v 98, no. 5, p. 2526-2532, doi: 10.1785/0120080107.

Wessel, P., and W.H.F Smith (1991), Free software helps map and display data. EOS, Transactions, American Geophysical Union 72. 441, 445-446.

Wolfe, C. J. and P. G. Silver, 1998. Seismic anisotropy of oceanic upper mantle: Shear-wave splitting observations and methodologies, *J. Geophy. Res.*, **103**, 749-771.

Wüstefeld, A., G. Bokelmann, C. Zaroli, and G. Barruol (2008), Splitlab: A shear-wave splitting environment in Matlab, Computers and Geosciences, 34(5), 515-528, doi: 10.1016/j.cageo.2007.08.002.

Zhang S, and S. Karato (1995), Lattice preferred orientation of olivine aggregates deformed in simple shear.Nature 415:777–780

Zimmerman, M.E., S. Zhang, D.L. Kohlstedt, and S. Karato (1999), Melt distribution in mantle rocks deformed in simple shear. Geophys. Res. Lett. 26, 1505–1508. doi: 10.1029/1999GL900259

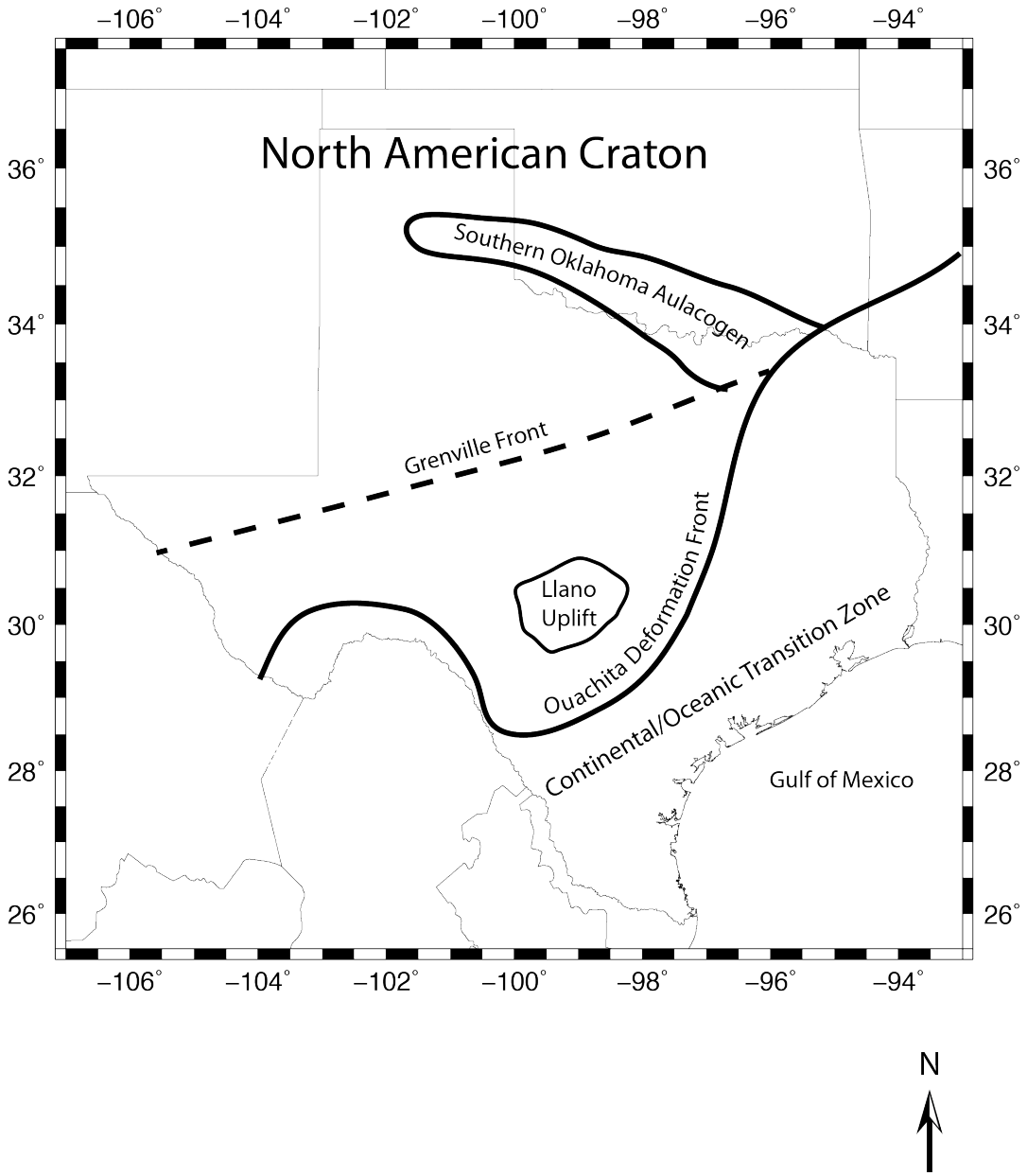

Figure 1. Map of the principal tectonic features of Texas and Oklahoma. Region I is defined by the Southern Oklahoma Aulacogen. Region II encompasses the stable North American craton up to the Ouachita deformation front and region III is defined south of the Ouachita deformation front to the Gulf of Mexico.

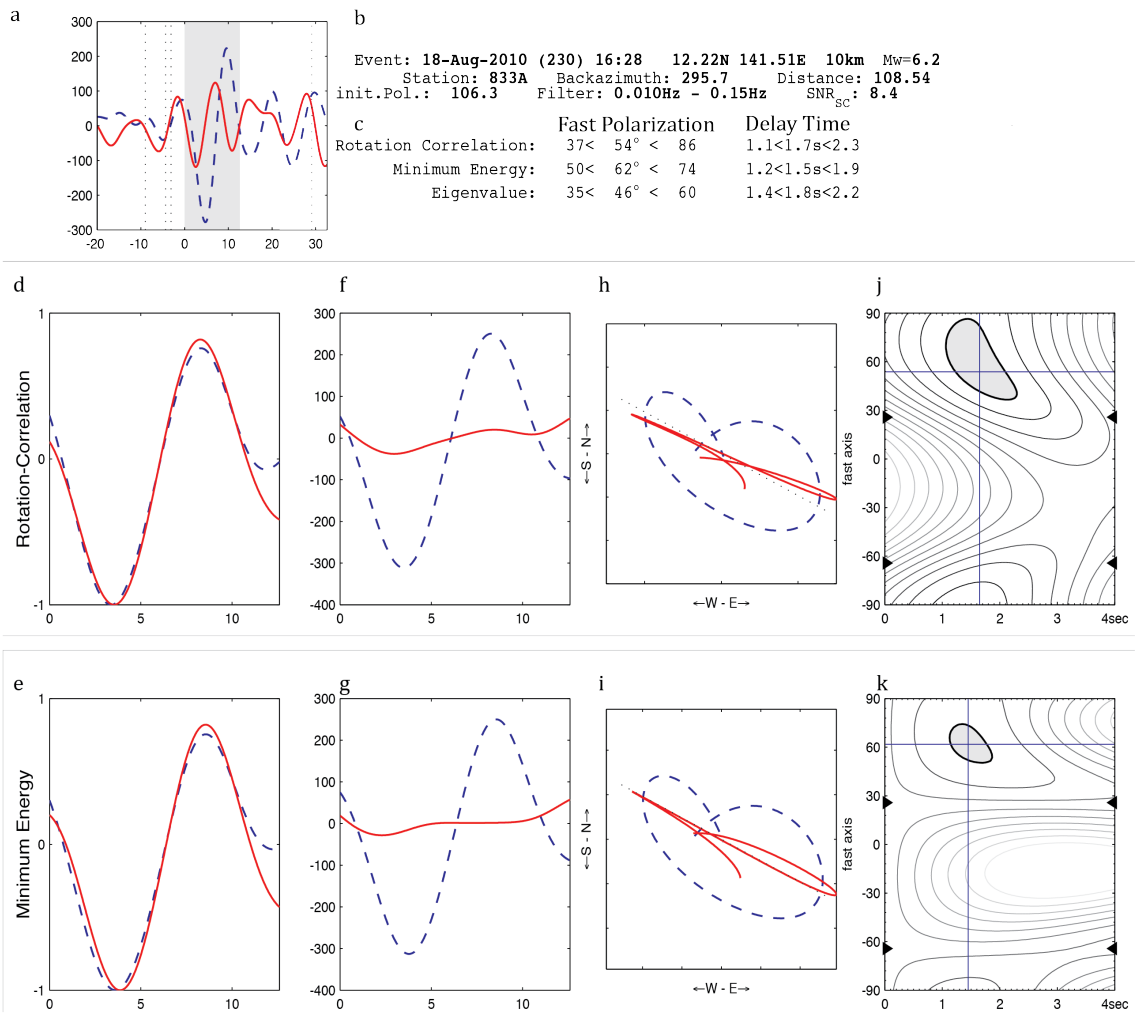

Figure 2. Diagnostic viewer in SplitLab of a good shear wave splitting measurement from station 833A. a) The selection of the fast (solid line) and slow (dashed line) shear wave components before the corrections are applied to the SKS arrivals. b) The text pane contains the header information for the event such as the date, location, magnitude, depth station name, back azimuth and distance in degrees from station. c) Splitting parameters results from all three techniques (RC, SC and EV). Each method provides the best estimate of polarization (ϕ) and delay time (δt) with error bounds of the confidence region. The RC and SC methods are displayed visually while the EV method is only shown numerically. (d, e) RC (d) and SC (e) delay corrections applied to the fast (solid line) and slow (dashed line); (f, g) RC (f) and SC (g) corrections applied to the radial (sold line) and transverse (dashed line) components; (h, i) particle motion of wave arrival before (dashed) and after (solid) the RC (h) and SC (i) corrections; (j, k) map of correlation coefficients with fast polarization directions (degrees) on the y-axis and delay time (seconds) on the x-axis for both the RC (j) method and SC (k).

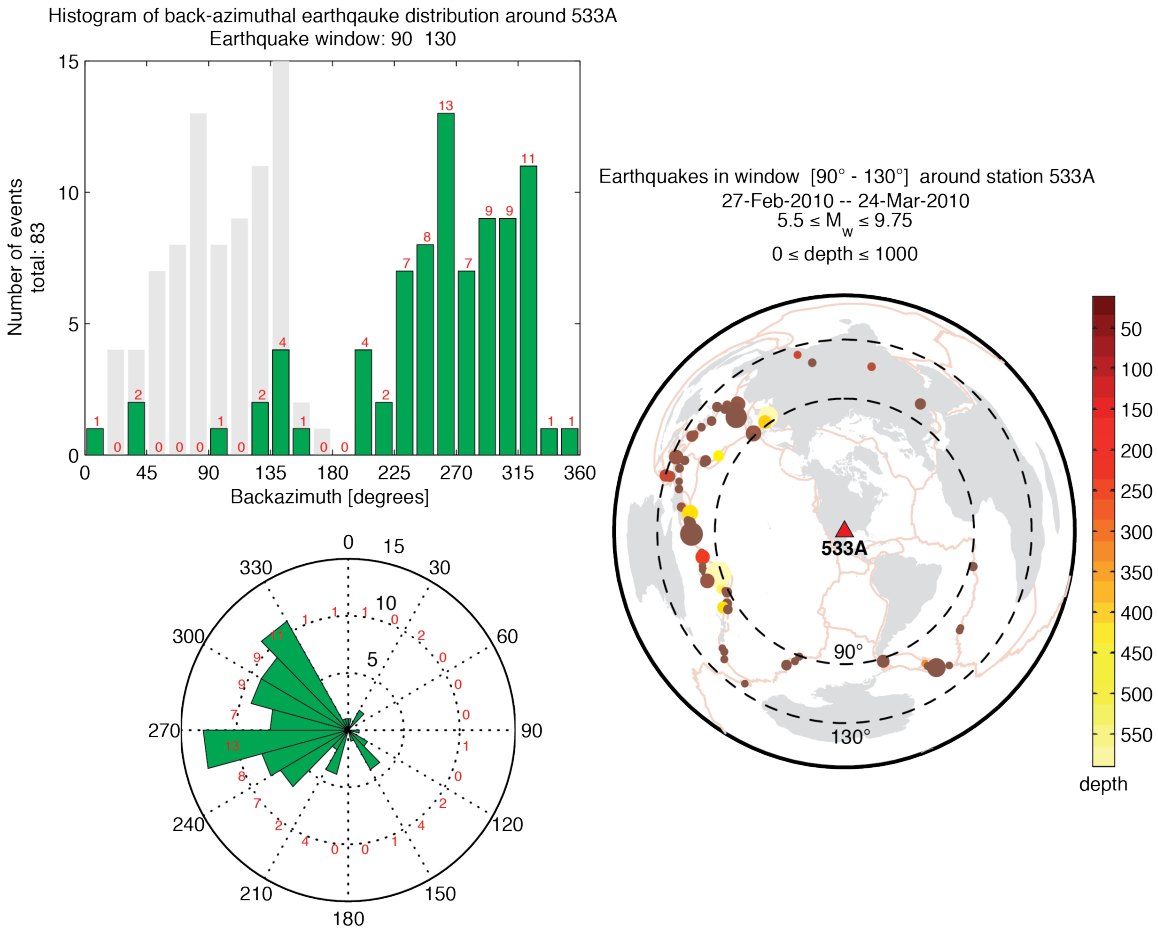

Figure 3. Back azimuths from earthquake events expressed as both a histogram (top left), a rose diagram (bottom left) and as a map showing event distribution and depths (top right).

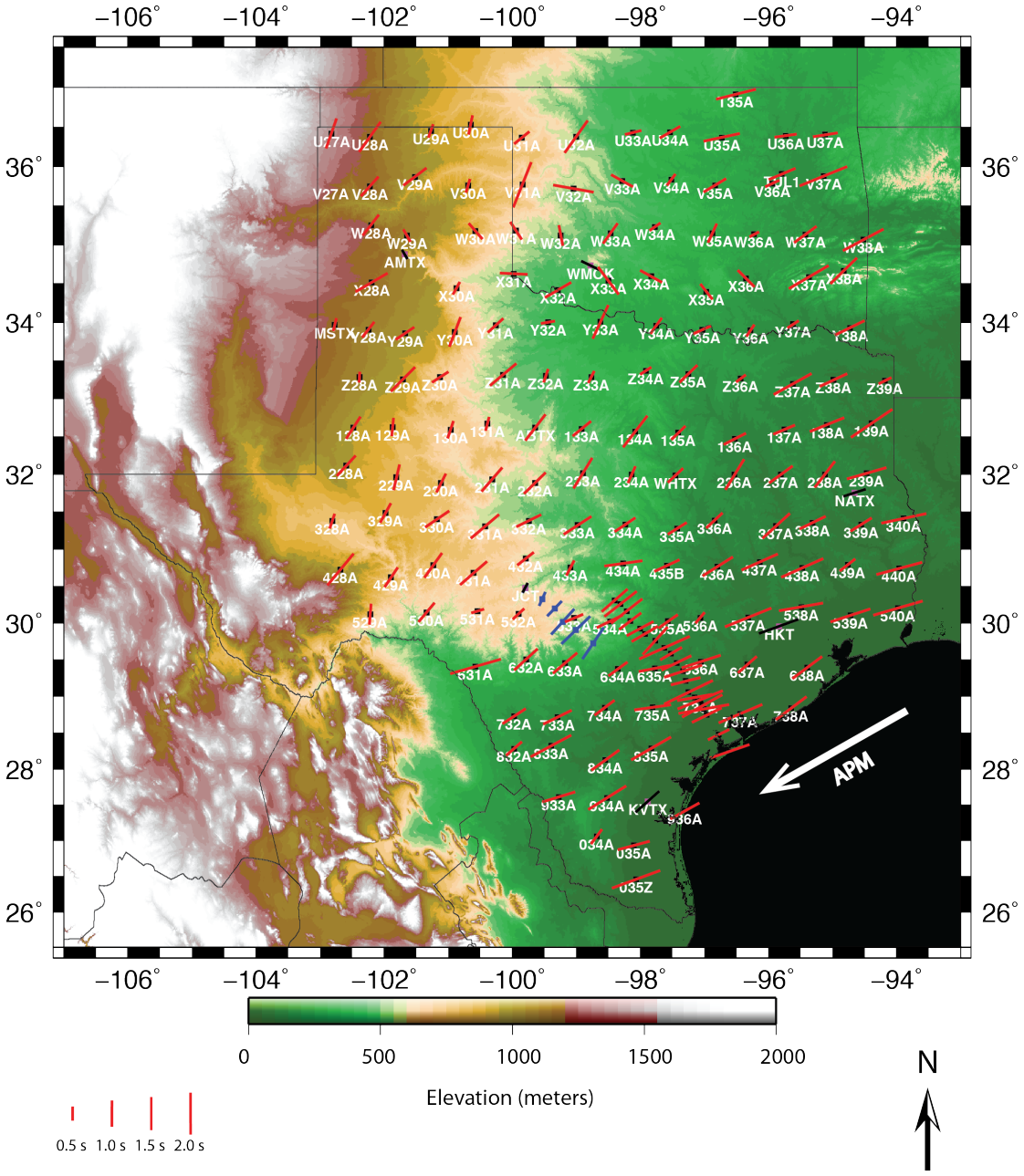

Figure 4. Map of study region with SKS measurements plotted as vectors representing δt, (in seconds) and ϕ, (the fast axis polarization direction measured clockwise from north, in degrees) for each station in the study region. Red splits are from current study; black splits are from Gao et al., 2008's study and blue splits are from Satsukawa et al., 2010's study. The average plate motion of the North American plate was calculated using the NNR model (DeMets et al., 2010).

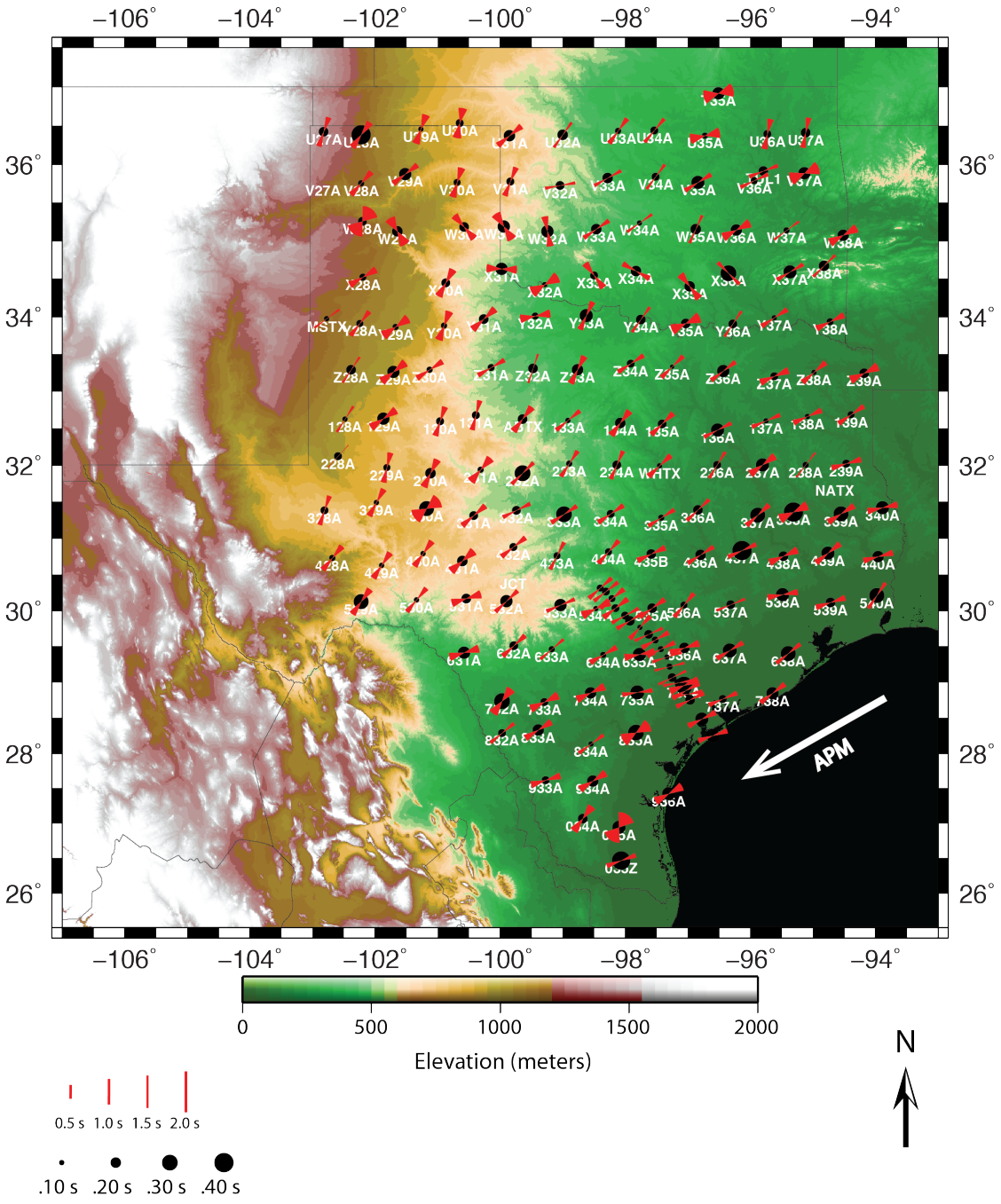

Figure 5. Map of SKS splitting measurement errors. Red error wedges indicate error in fast axis polarization direction and black circles show delay time error. Errors on both parameters were calculated using a 95% confidence interval.

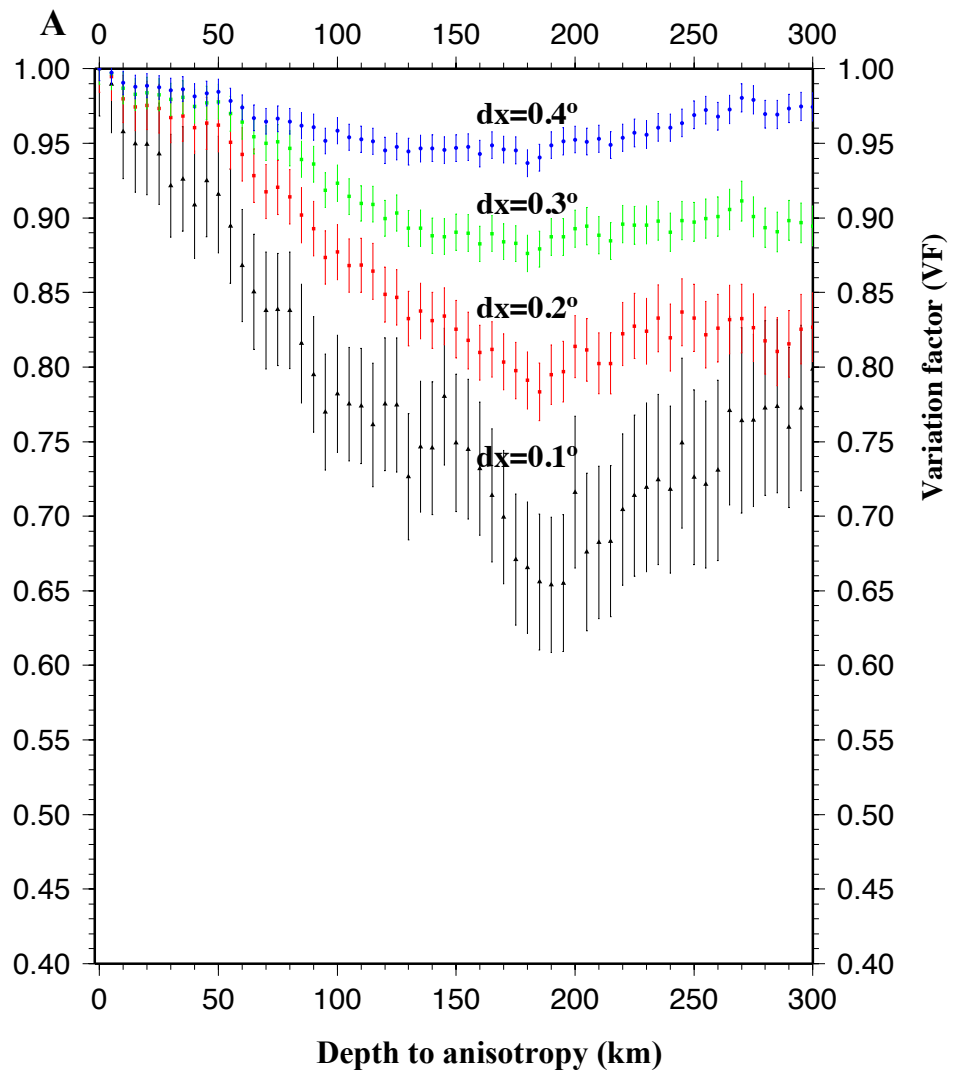
A
0
50
100
150
200
250
300
1.00
0.95
0.90
0.85
0.80
0.75
0.70
0.65
0.60
0.55
0.50
0.45
0.40
dx=0.4º
dx=0.3º
dx=0.2º
dx=0.1º
Variation factor (VF)
Depth to anisotropy (km)

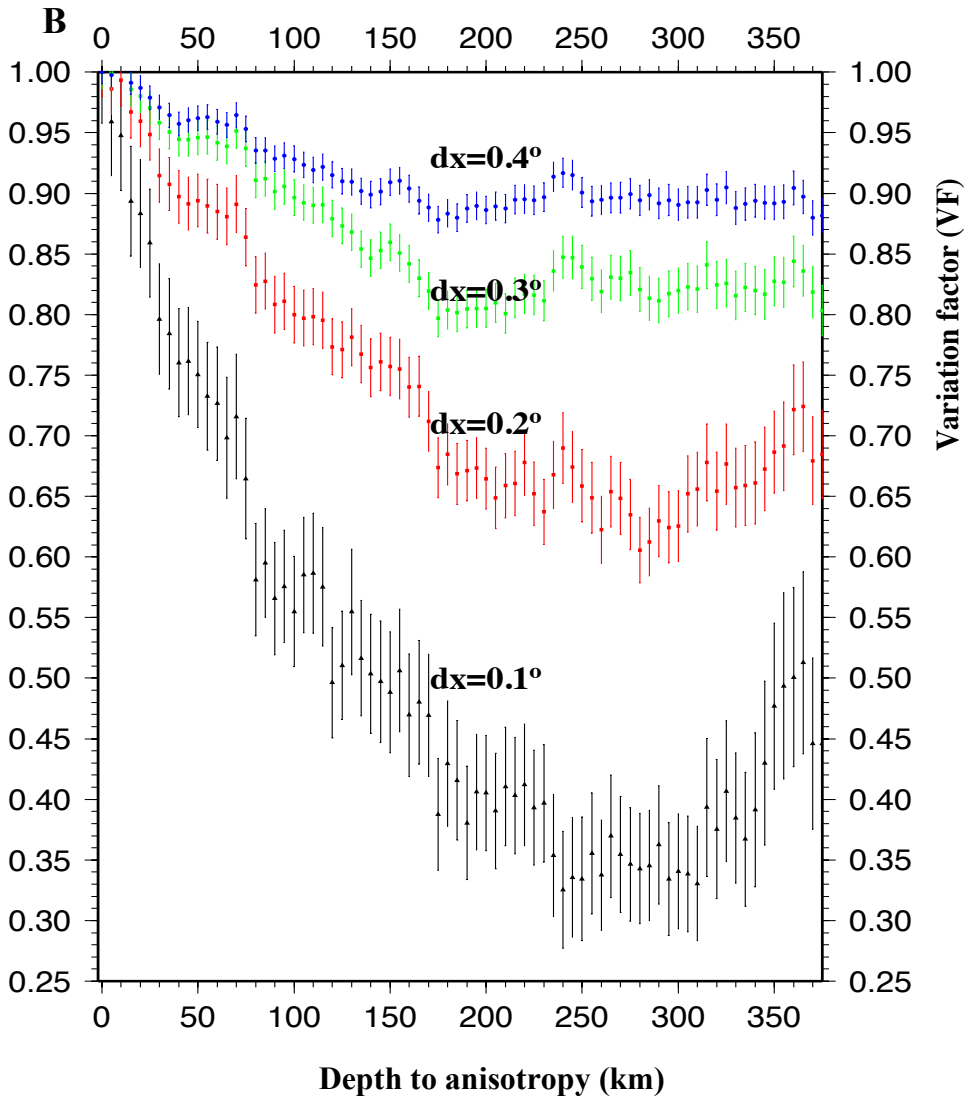

Figure 6. Results from AnisDep (a) stations located on the craton (b) stations located on the continental-oceanic transition zone. A layer of anisotropy corresponds to a minimum on the graph for each bin spacing size (1°- 4°). A layer of anisotropy at 180 km best fits measurements made at stations located on the craton; a layer of anisotropy at 280 km best fits measurements made at stations on the continent-ocean transition zone.

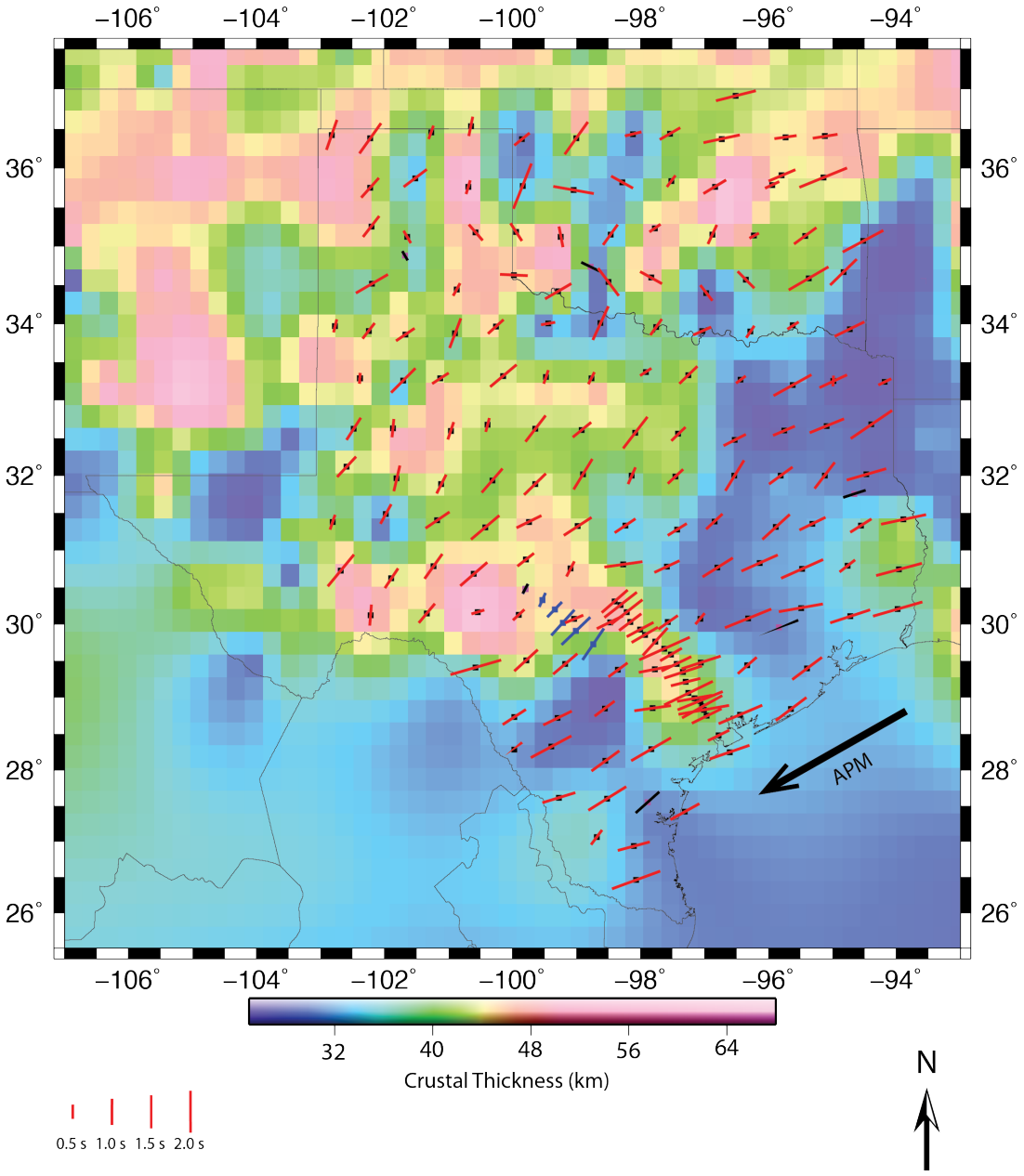

Figure 7. EarthScope Automated Receiver function Study (EARS) map showing both the average crustal thickness for Texas and Oklahoma

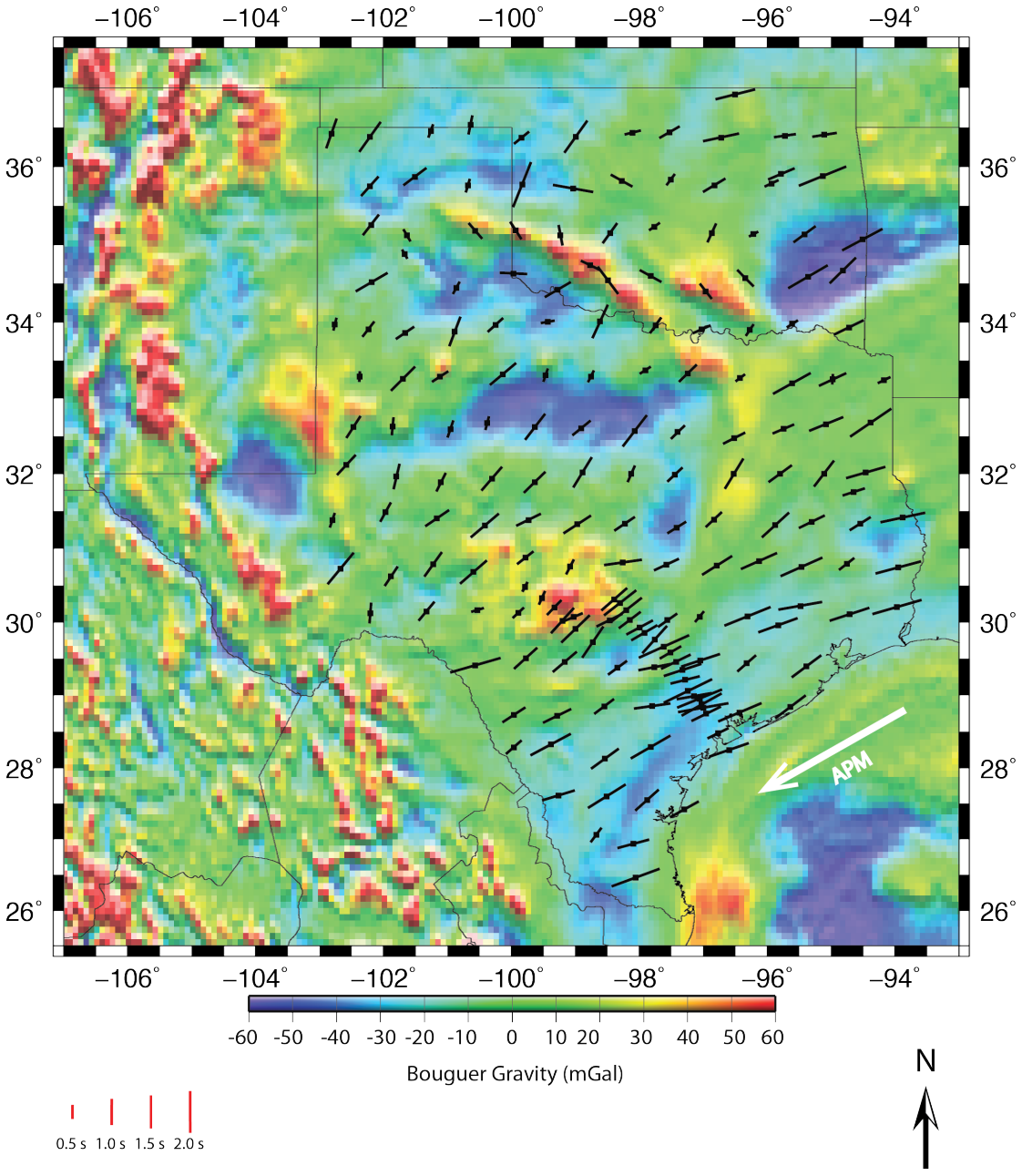

Figure 8. Gravity map of Texas and Oklahoma overlain with SKS measurements

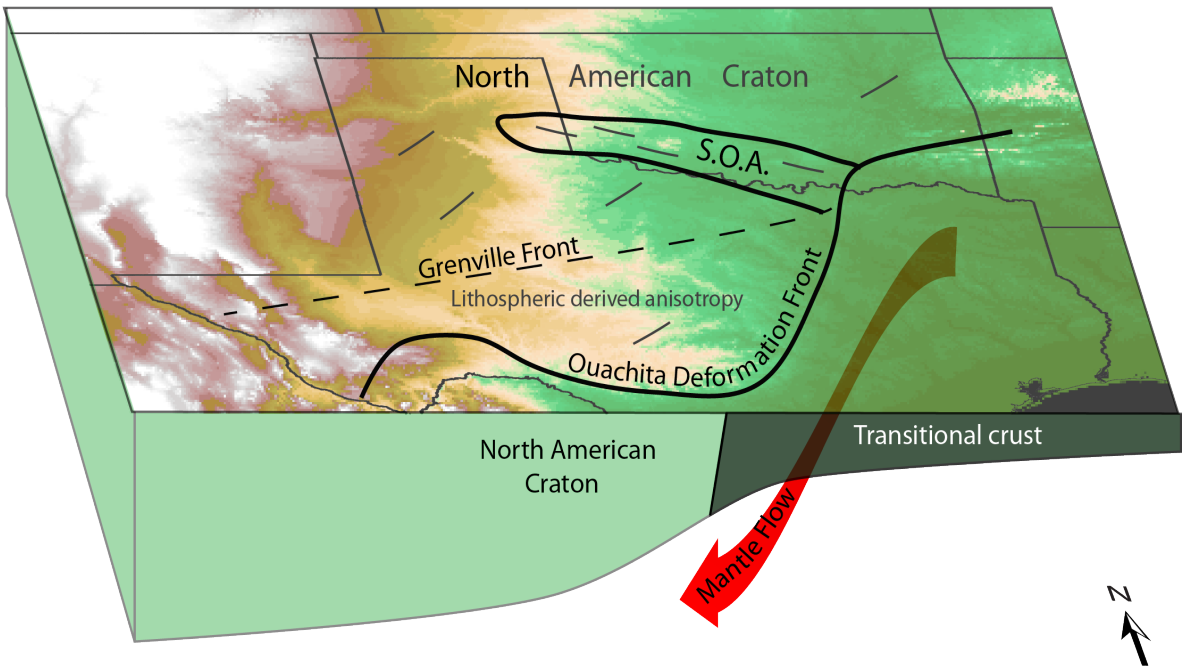

Figure 9. Cartoon model of seismic anisotropy from SKS splitting measurements. This cartoon depicts the type of anisotropy for each of the three regions explained in this study. Seismic anisotropy beneath region I is likely defined by a combination of shearing from the movement of the North American plate and contributions from fossil anisotropy. Region II's seismic anisotropy is most likely due to the formation of rift-parallel magmatic dikes that define the high gravity province of the Southern Oklahoma Aulacogen. Along the continental-oceanic transition zone of region III, seismic anisotropy is attributed to mantle flow around the keel of the North American craton.

CHAPTER THREE

Conclusions

From the results gathered by this study, a more detailed understanding is presented on the deep Earth structure of Texas and Oklahoma. The introduction of the EarthScope TA stations into the region had brought about a revolution in our understanding of the deep Earth structures beneath Texas and Oklahoma. This geophysical study and others that are ongoing at Baylor will resolve some of the more intriguing scientific questions of the region and hopefully open up new questions that further students at Baylor can tackle.

APPENDIX

APPENDIX A

Appendix A: Table of Shear Wave Splitting Measurements

Table 1
Shear wave splitting measurements

Station ID	Latitude	Longitude	Events used	Phi	Phi error	Dt	Dt error	Location
034A	27.0647	-98.6833	4	36.7	± 16.7	0.7	± 0.10	COTZ
035A	26.9379	-98.1023	2	74.92	± 6.73	1.25	± 0.25	COTZ
035Z	26.463	-98.0683	3	69.7	± 9.76	1.95	± 0.35	COTZ
129A	32.6309	-101.866	2	5.53	± 1.01	0.7	± 0.23	Craton
133A	32.6083	-98.9162	2	50.78	± 8.43	0.9	± 0.14	Craton
134A	32.5729	-98.0795	3	37.42	± 14.22	1.5	± 0.21	Craton
135A	32.5573	-97.4099	2	45.75	± 10.45	0.75	± 0.17	Craton
Z38A	33.2884	-102.386	3	3.52	±1.08	0.4	± 0.08	COTZ
136A	32.4746	-96.5297	3	62.85	± 8.16	0.95	± 0.26	COTZ
128A	32.6213	-102.485	3	32.68	± 5.23	1	± 0.11	Craton
Z35A	33.3308	-97.253	1	45.75	± 9.8	0.95	± 0.18	Craton
228A	32.1181	-102.591	2	42.74	± 6.19	1.05	± 0.15	Craton
229A	31.9671	-101.81	3	13.15	± 1.85	1	± 0.14	Craton
230A	31.8878	-101.112	3	26.65	± 9.47	0.8	± 0.20	Craton
231A	31.9353	-100.316	3	40.73	± 17.02	1.2	± 0.12	Craton
232A	31.8881	-99.6469	4	45.51	± 8.17	1.15	± 0.30	Craton
233A	32.0179	-98.8998	3	31.35	± 9.29	1.35	± 0.22	Craton
237A	32.0015	-95.8084	5	53.8	± 15.28	1.1	± 0.28	COTZ
238A	32.0034	-95.1203	2	37.42	± 4.83	1.25	± 0.18	COTZ
239A	32.0179	-94.4707	2	73.82	± 11.72	1.55	± 0.15	COTZ
329A	31.487	-101.98	2	28.66	± 9.31	0.85	± 0.11	COTZ
330A	31.4063	-101.175	2	55.6	±19.5	1.1	± 0.29	Craton
331A	31.3085	-100.426	2	49.55	± 12.11	1.4	± 0.17	Craton

(continued)

333A	31.3249	98.9841	5	56.82	± 9.29	1.25	± 0.31	Craton
334A	31.3325	98.2379	5	55.91	± 10.40	0.95	± 0.16	Craton
338A	31.3567	95.3106	3	63.85	± 18.93	1.1	± 0.37	Craton
339A	31.3331	-94.556	2	57.64	± 12.54	0.95	± 0.28	Craton
340A	31.4167	93.8896	1	77.87	± 12.76	1.75	± 0.25	Craton
429A	30.6248	101.893	2	33.69	± 9.92	0.9	± 0.14	Craton
430A	30.7866	101.236	2	35.39	± 12.8	1.15	± 0.11	Craton
431A	30.6824	100.607	2	48.77	± 17.7	1.35	± 0.20	Craton
432A	30.8755	99.7937	2	51.79	± 10.42	0.8	± 0.16	Craton
433A	30.7544	-99.091	2	27.3	± 8.26	0.65	± 0.13	COTZ
437A	30.8292	96.1386	3	65.87	± 9.33	1.5	± 0.32	COTZ
438A	30.7501	95.4741	2	65.87	± 14.55	1.75	± 0.19	COTZ
439A	30.7937	-94.766	3	51.79	± 12.31	0.75	± 0.26	COTZ
440A	30.7456	93.9587	1	74.92	± 11.95	1.8	± 0.22	COTZ
532A	30.1278	99.9049	2	46.76	± 8.88	0.6	± 0.23	Craton
533A	30.0718	99.0351	1	66.87	± 7.83	0.75	± 0.19	Craton
534A	30.0284	98.4753	2	63.71	± 16.89	1.1	± 0.17	Craton
535A	30.029	97.5711	1	54.8	± 10.6	0.9	± 0.18	COTZ
536A	30.0756	97.0652	4	39.72	± 9.45	0.55	± 0.14	COTZ
537A	30.0799	96.3155	1	67.88	± 5.45	1.9	± 0.12	COTZ
538A	30.2219	-95.49	8	79.94	± 12.15	1.7	± 0.26	COTZ
540A	30.2093	93.9796	3	73.82	± 17.54	1.95	± 0.28	COTZ
631A	29.4123	100.575	1	73.82	± 15.95	2	± 0.23	Craton
633A	29.4591	99.1766	2	49.55	± 6.25	1.2	± 0.12	Craton

(continued)

634A	29.3815	98.3515	2	53.6	± 11.29	0.9	± 0.16	Craton
636A	29.481	-97.057	2	71.8	± 13.97	1.55	± 0.20	COTZ
637A	29.439	96.3324	4	48.6	± 9.97	0.95	± 0.27	COTZ
732A	28.7292	99.9707	3	56.7	± 11.87	1.05	± 0.30	Craton
733A	28.7192	99.2939	2	63.71	± 16.57	1.2	± 0.15	Craton
734A	28.8473	98.5576	2	52.79	± 15.46	0.95	± 0.22	Craton
735A	28.8553	97.8081	2	81.91	± 9.02	1.4	± 0.27	Craton
736A	28.955	97.0673	3	67.75	± 14.55	1.85	± 0.34	COTZ
738A	28.8404	95.6481	2	52.79	± 10.79	1.45	± 0.24	COTZ
832A	28.2844	99.9743	1	48.66	± 7.64	0.8	± 0.15	Craton
833A	28.3236	99.3939	2	61.69	± 13.18	1.75	± 0.22	Craton
835A	28.287	97.8297	2	59.83	± 22.12	1.75	± 0.31	COTZ
934A	27.6018	98.5192	2	57.82	± 14.97	1.7	± 0.22	COTZ
936A	27.4208	97.3091	2	60.84	± 17.02	1.25	± 0.26	COTZ
ABTX	32.6238	99.6431	3	37.42	± 14.22	1.25	± 0.18	Craton
U29A	36.4519	-101.27	2	19.61	± 9.55	0.55	± 0.11	Craton
U30A	36.5304	-100.65	3	11.51	± 6.85	0.75	± 0.16	Craton
T35A	36.9161	96.5121	3	75.84	± 22.78	1.55	± 0.24	Craton
TUL1	35.9104	95.7919	2	66.88	± 7.95	1.1	± 0.19	Craton
V30A	35.7623	100.689	2	16.59	± 14.60	0.55	± 0.13	Craton
V31A	35.7739	99.8425	4	21.62	± 11.45	1.85	± 0.15	Craton
U35A	36.3709	96.7318	2	77.87	± 20.56	1.4	± 0.21	Craton
V28A	35.7505	102.224	3	41.73	± 12.25	1	± 0.13	Craton

(continued)

V29A	35.8734	-101.52	2	52.79	± 11.69	1.1	± 0.23	Craton
W28A	35.2574	102.206	2	37.71	± 7.24	1	± 0.17	SOA
W29A	35.1212	101.647	2	-30	± 21.05	0.55	± 0.20	SOA
V32A	35.7202	99.0437	3	-79.89	± 6.22	1.55	± 0.17	Craton
V34A	35.8345	-97.517	3	36.54	± 6.23	0.55	± 0.15	Craton
V35A	35.7626	-96.837	1	58.83	± 9.76	1	± 0.26	Craton
V37A	35.883	-95.141	2	67.75	± 11.87	1.95	± 0.24	Craton
W36A	35.1393	96.2264	4	61.84	± 17.86	0.4	± 0.22	Craton
W37A	35.138	95.4269	3	53.6	± 4.59	1.05	± 0.12	Craton
W31A	35.1864	99.9435	2	-32.75	± 19.33	0.8	± 0.23	SOA
638A	29.4	-95.4	3	53	± 8.54	1.4	± 0.28	COTZ
W32A	35.1238	99.2458	3	-10.78	± 17.35	0.8	± 0.21	SOA
W34A	35.2352	97.7733	2	54.8	± 5.70	0.5	± 0.11	Craton
W35A	35.1527	96.8745	2	24.64	± 5.99	0.8	± 0.20	Craton
X35A	34.3995	96.9731	3	-37.85	± 15.37	0.75	± 0.21	SOA
X36A	34.5704	-96.352	3	-44.75	± 7.91	0.9	± 0.30	SOA
W38A	35.0704	94.5184	3	61.84	± 17.52	1.75	± 0.22	Craton
WHTX	31.9913	97.4561	3	46.76	± 11.72	0.8	± 0.11	Craton
X31A	34.6309	99.9793	3	-87.22	± 16.19	1.05	± 0.23	SOA
X32A	34.4214	99.2854	3	59.66	± 12.59	1.15	± 0.21	SOA
X37A	34.5892	95.3713	2	59.66	± 8.46	1.75	± 0.26	Craton
X38A	34.6692	94.8288	1	45.51	± 5.87	1.4	± 0.20	Craton
Y28A	33.9086	102.247	4	37.71	± 9.92	0.75	± 0.14	Craton
Y30A	33.8766	100.897	3	20.61	± 15.59	1.2	± 0.16	Craton
Z29A	33.2595	101.706	2	44.75	± 17.08	1.3	± 0.24	Craton
Z28A	33.2884	102.386	3	3.52	± 4.67	0.4	± 0.18	Craton

(continued)

236A	31.9997	-96.531	2	31.35	± 6.49	1.35	± 0.22	COTZ
Y35A	33.9059	97.0374	3	65.87	± 21.39	0.75	± 0.19	Craton
Y36A	33.8996	96.2848	2	33.69	± 5.59	0.55	± 0.17	Craton
Y37A	33.9789	-95.621	2	56.82	± 10.14	0.5	± 0.11	SOA
Z37A	33.1981	95.6229	4	60.84	± 14.18	1.65	± 0.18	COTZ
Z38A	33.2499	94.9851	4	64.86	± 11.33	1.15	± 0.15	COTZ
Z31A	33.3183	100.143	3	49.83	± 9.88	1.3	± 0.16	Craton
Z33A	33.2865	98.7648	3	26.56	± 13.51	0.5	± 0.22	Craton
Z34A	33.3712	97.9158	5	56.82	± 10.97	0.5	± 0.16	Craton
Z36A	33.2702	96.4344	5	52.79	± 9.36	0.45	± 0.21	Craton
Z39A	33.2418	94.1822	3	63.85	± 17.43	0.55	± 0.18	COTZ
139A	32.6795	94.3927	2	55.62	± 10.27	1.9	± 0.14	COTZ
130A	32.5961	100.965	4	18.6	± 11.98	0.7	± 0.16	Craton
131A	32.6737	100.388	2	14.58	± 10.35	0.55	± 0.15	Craton
137A	32.5973	95.7559	3	66.87	± 8.82	0.9	± 0.13	COTZ
138A	32.6604	95.0887	2	67.75	± 11.26	1.4	± 0.11	COTZ
328A	31.3818	102.809	1	18.6	± 9.79	0.6	± 0.09	Craton
234A	32.004	98.1368	2	23.63	± 9.07	0.7	± 0.17	Craton
428A	30.7263	102.684	2	39.44	± 12.44	1.55	± 0.10	Craton
332A	31.3829	99.7423	3	63.71	± 8.25	1.05	± 0.14	Craton
335A	31.2819	97.4271	4	57.82	± 8.85	0.85	± 0.17	Craton
336A	31.387	96.8443	3	46.76	± 10.98	0.85	± 0.13	Craton
337A	31.3159	95.8854	4	47.42	± 12.25	1.4	± 0.20	COTZ
434A	30.8142	-98.269	2	81.91	± 14.06	1.45	± 0.15	Craton
435B	30.7827	-97.585	4	64.86	± 2.12	1.05	± 0.27	Craton

(continued)

436A	30.7702	-96.796	4	57.64	± 14.97	1.35	± 0.14	COTZ
635A	29.3877	97.7736	2	78.94	± 17.02	1.25	± 0.11	COTZ
531A	30.1645	100.546	5	72.91	± 14.22	0.5	± 0.26	Craton
539A	30.1084	94.7236	5	71.8	± 9.55	1.6	± 0.22	COTZ
632A	29.5071	99.7863	5	47.53	± 6.85	1.2	± 0.29	Craton
933A	27.6133	99.2746	2	72.91	± 22.78	1.3	± 0.11	COTZ
737A	28.7639	96.4402	5	66.87	± 7.95	1.8	± 0.23	COTZ
834A	28.1251	98.5519	4	53.8	± 11.02	1.3	± 0.19	COTZ
U33A	36.4327	98.1135	5	75.92	± 13.87	0.65	± 0.17	Craton
MSTX	33.9696	102.772	2	13.58	± 14.60	0.5	± 0.18	Craton
U36A	36.3927	95.7325	2	81.96	± 11.45	0.85	± 0.14	Craton
U31A	36.3695	99.8508	2	50.78	± 20.56	0.75	± 0.12	Craton
U32A	36.3795	99.0014	2	35.39	± 12.25	1.5	± 0.26	Craton
V36A	35.7863	95.9425	4	64.86	± 11.69	0.6	± 0.13	Craton
U34A	36.4365	97.5354	2	59.83	± 7.66	0.9	± 0.15	Craton
W33A	35.1518	98.4686	2	35.62	± 10.67	0.95	± 0.13	Craton
U37A	36.406	95.1161	2	80.95	± 14.56	0.95	± 0.16	Craton
V33A	35.8209	98.2862	3	-60.84	± 16.19	0.95	± 0.22	Craton
X33A	34.541	98.5006	2	-36.7	± 11.26	1.3	± 0.08	Craton
W30A	35.1818	100.577	2	-40.74	± 13.67	0.8	± 0.06	SOA
Y29A	33.8602	101.671	2	55.81	± 9.07	0.85	± 0.14	Craton
X23A	34.5185	102.197	4	59.66	± 10.03	1.4	± 0.10	Craton
X30A	34.4461	100.874	2	28.66	± 11.07	0.55	± 0.11	Craton
Z38A	33.2499	94.9851	2	3.52	± 7.89	0.4	± 0.12	COTZ
X34A	34.601	97.8326	3	-60.92	± 15. 22	0.95	± 0.13	Craton

(continued)

Z32A	33.3066	99.4783	4	18.6	± 8.13	0.55	± 0.19	Craton
Y32A	34.0036	-99.442	2	79.94	± 12.14	0.55	± 0.22	Craton
Y38A	33.9278	94.7311	2	63.85	± 16.89	1.25	± 0.08	Craton
GC01	28.2472	96.6062	2	70.89	± 10.65	1.6	± 0.11	COTZ
GC03	28.4777	96.7764	2	63.74	± 11.55	1.6	± 0.15	COTZ
GC05	28.7467	96.9667	3	63.71	± 9.33	1.62	± 0.23	COTZ
GC06	28.8759	97.0345	2	60.73	± 10.22	1.75	± 0.21	COTZ
GC07	28.9871	97.1551	4	79.94	± 6.39	1.65	± 0.16	COTZ
GC08	29.06	97.2505	4	63.85	± 5.28	2.05	± 0.22	COTZ
GC09	29.2135	97.2929	4	75.84	± 12.46	1.3	± 0.13	COTZ
GC10	29.3485	97.3376	2	71.9	± 14.33	1.5	± 0.09	COTZ
GC11	29.459	97.4368	2	63.93	± 10.19	1.25	± 0.18	COTZ
GC12	29.5871	97.5226	5	59.66	± 6.87	1.15	± 0.14	COTZ
GC13	29.669	97.6274	2	65.73	± 14.87	1.32	± 0.17	COTZ
GC14	29.7641	97.7709	2	41.8	± 11.38	1.28	± 0.10	COTZ
GC15	29.8579	97.9316	3	59.66	± 11.22	1.15	± 0.11	COTZ
GC16	29.9304	98.0072	2	61.69	± 15.33	1.15	± 0.16	COTZ
GC17	30.0323	98.1602	3	52.79	± 11.11	1.05	± 0.21	COTZ
GC18	30.1664	-98.213	2	51.8	± 9.02	0.83	± 0.12	COTZ
GC19	30.262	-98.31	2	51.84	± 6.33	0.8	± 0.11	Craton
GC20	30.3099	98.4044	2	48.72	± 11.87	0.72	± 0.14	Craton
GC24	28.8301	97.0106	3	79.89	± 10.32	0.75	± 0.15	Craton